

Flow instability prediction via eigenanalysis and its application to rotating stall

Shenren Xu ^{*1,2}, Chen He^{†3}, Dakun Sun^{‡3}, and Dingxi Wang^{§ 2}

¹*Yangtze River Delta Research Institute of NPU, Northwestern Polytechnical University, Taicang 215400, P.R. China*

²*Northwestern Polytechnical University, Xi'an 710072, P.R. China*

³*Beihang University, Beijing 100191, P.R. China*

Global linear stability analysis is an effective way to predict the exact condition at which flow goes unstable. Compared to the time-domain simulation approach, eigenanalysis method can equivalently predict the destabilization condition, but at a much lower cost, since unsteady simulations are no longer required. In this work, a Newton–Krylov nonlinear flow solver is used to first solve for the steady state flow solution and then eigenanalysis is performed by applying the implicit-restart Arnoldi method to the exact Jacobian matrix. By tracking a subset of the eigenspectrum that is close to the imaginary axis, the least stable eigenmodes can be found. By perturbing the bifurcation parameter, e.g., the Reynolds number, the Hopf bifurcation point can be identified. This method is applied to find the critical Reynolds number for a laminar flow around a circular cylinder above which laminar vortex shedding appears. Time-accurate unsteady simulation confirms the correctness of the critical eigenvalue and eigenvector found. It is also applied to a quasi-3D compressor rotor annular cascade case, for which eigenanalysis is performed and flow physics is analyzed based on the unstable modes identified. Interesting correlation between the rotating perturbation pattern and cell rotating speed is found, which resembles what is observed in experiments. This work is a first step towards the study of rotating flow instabilities in turbomachines, such as rotating stall and rotating instability, and the preliminary results proved promising for future application to three-dimensional practical problems.

I. Introduction

Rotating stall and rotating instability have been studied extensively both experimentally [1–3] and numerically [4–7]. Early experimental work revealed the basic features of such phenomenon and subsequent work has focused on building simple analytical models. Existing analytical models [1, 8] have had their success in the early days but the accuracy and

*Associate Professor, School of Power and Engery; shenren_xu@nwpu.edu.cn

†Ph.D. Candidate, School of Energy and Power Engineering; hechen@ buaa.edu.cn (Corresponding Author)

‡Associate Professor, School of Energy and Power Engineering; Co-Innovation Center for Advanced Aero-Engine; sundk@buaa.edu.cn

§Professor, School of Power and Engery; dingxi_wang@nwpu.edu.cn

effectiveness of them is less than satisfactory when applied to realistic configurations and more details are needed for quantitative prediction of the stall behavior.

Previous numerical investigations mainly focused on using time-dependent unsteady flow analysis using either a fraction or the whole of an annulus. A lot of insight into the flow physics for the destabilization mechanism has been gained from such high fidelity simulations. Unsteady simulations are useful for both reproducing the fully destabilized unsteady flows as well as for studying the inception of such instability. Due to the high computational cost of unsteady simulation, it still remains largely as a research tool to investigate the stall phenomenon on a case-by-case basis.

It is widely believed that the fully developed stall and surge behavior is quite different from the incipient stall, or pre-stall disturbance [9], as fully developed rotating stall exhibits strong nonlinearity. However, if the goal is to apply active control to suppress the instability at its infancy, then a linear stability prediction should suffice, as has been demonstrated in numerous work [10–13], as the idea is to eliminate the fully-developed rotating cells from forming.

As modern compression systems are designed with higher loading and speed, most analytical models proposed in the early days and demonstrated useful on low-speed machines are no longer useful as compressibility and complex flow mechanism such as boundary-layer-shock-wave interaction becomes important. In addition, existing models seldom take into account the exact geometry of the blading, and instead, a simple correlation of the compressor characteristics is used. This is obviously not desirable as geometry details, such as the exact leading edge geometry, have great impact on the stall characteristics. This is particularly the case when more complex stall phenomenon are considered, such as spike stall, where geometry details such as tip gap and the leading edge shape play a major role.

This calls for a stability analysis method based on the three-dimensional Reynolds-averaged Navier-Stokes equations, which is regarded as the standard industrial tool for predicting steady and unsteady turbomachinery performance. In a way, existing stall model needs to be upgraded using the latest high-fidelity flow models. Again, either time-dependent simulations or steady-state-based eigenanalysis can be used to study the stability based on the high-fidelity models and each has its strength. Time-dependent analysis is able to capture not only the incipient stall behavior but also the details of the transient process, but at a very high computational cost. Eigenvalue analysis is a powerful yet inexpensive tool to probe the flow near the critical condition, but is still capable of revealing rich flow physics, with cost comparable to a few steady state analysis.

In this work, we demonstrate that using eigenanalysis based on a whole-annulus steady state solution, the linear stability demarcation point can be pinpointed with the cost of a few steady state analysis, and a full-annulus time-accurate unsteady calculation can thus be avoided. This methodology enables quick parametric study of the various rotating flow instability phenomenon such as rotating stall and rotating instability.

The idea of performing such eigenanalysis is simple. The difficulty is in the detail. One common misunderstanding is that an eigenanalysis for large cases is expensive. This is true only if we were to compute the full spectrum of a large sparse linear system using a direct method [14]. However, since a subset of the millions or even billions of eigenvalues

are relevant regarding the linear stability, typically $O(100)$, such eigenanalysis can be done at the cost of a few steady state analysis, using iterative eigenvalue calculation methods [15, 16].

In practice, such eigenanalysis is rarely done for large, complex cases of industry relevance. The challenge is twofold. First, in order to perform eigenanalysis, a steady state flow solution should first be obtained, requiring the full convergence of the flow solver. While this is easily achievable at design condition, obtaining a fully converged solution at off-design conditions remains a challenge from the perspective of flow solver [17]. This is seldom discussed in literature, but widely felt in industry. Secondly, it is a common belief that the computational cost of such eigenanalysis is overwhelming and is thus impractical for real applications. With the maturing of distributed computing, this is no longer the bottleneck and one can easily compute the relevant eigenvectors for cases with up to 10 million grid point, and the cost only increases linearly with a scalable algorithm. But here the focus shifts slightly to the computational methods side from the flow physics. As discussed in [18], combining the advancement by computational specialists and the expertise from the ‘stall fraternity’ is the right way to advance the research in compressor stall study and an effective way to harness better the benefit of using CFD. In this paper, we attempt to apply the latest development in large scale eigenanalysis computational method to the long-standing problem of rotating flow instability, rotating stall in particular, and try to explore the underlying flow physics governing the pre- and in-stall behavior, at a computational cost that is affordable for industrial applications.

The rest of this paper is organized as follows. First, the basic algorithm of the nonlinear flow solver will be discussed in sec. II. Fundamentals of performing eigenanalysis based on RANS equations and relevant techniques are discussed in sec. III. Results for the application of eigenanalysis to predict flow instability is elaborated in sec. IV and conclusions are drawn in sec. V.

II. The nonlinear flow solver

The nonlinear flow solver used in this work is NutsCFD, an unstructured-mesh finite-volume RANS solver capable of dealing with rotating frame reference and periodic boundary conditions. The solver features the use of the Newton–Krylov algorithm, which significantly enhances the efficiency and robustness when computing turbomachinery flows at off-design conditions. Details of the solver can be found in [19] and a brief description of the solution algorithm is provided in this section.

A. Governing equations

The integral form of the governing equations in a relative frame of reference with a constant angular velocity of ω is

$$\frac{d}{dt} \int_{\Omega_r} \mathbf{W} dV + \oint_{\partial\Omega_r} (\mathbf{F}_c^r - \mathbf{F}_v) dS + \int_{\Omega_r} \mathbf{F}_\omega dV = 0,$$

where \mathbf{W} are the conservative variables $[\rho, \rho\mathbf{u}, \rho E]^T$. The absolute and relative convective fluxes, \mathbf{F}_c and \mathbf{F}_c^r , the viscous flux \mathbf{F}_v , and the additional source term due to rotation, \mathbf{F}_ω , are defined as

$$\mathbf{F}_c = \begin{bmatrix} \rho\mathbf{u} \cdot \mathbf{n} \\ \rho\mathbf{u}\mathbf{u} \cdot \mathbf{n} + p\mathbf{n} \\ \rho H\mathbf{u} \cdot \mathbf{n} \end{bmatrix}, \quad \mathbf{F}_c^r = \mathbf{F}_c - (\mathbf{u}_{rot} \cdot \mathbf{n}) \begin{bmatrix} \rho \\ \rho\mathbf{u} \\ \rho E \end{bmatrix}, \quad \mathbf{F}_v = \begin{bmatrix} 0 \\ \boldsymbol{\tau} \cdot \mathbf{n} \\ \mathbf{u} \cdot \boldsymbol{\tau} \cdot \mathbf{n} + \kappa\mathbf{n} \cdot \nabla T \end{bmatrix}, \quad \mathbf{F}_\omega = \begin{bmatrix} 0 \\ \rho\boldsymbol{\omega} \times \mathbf{u} \\ 0 \end{bmatrix},$$

with $\mathbf{u}_{rot} = \boldsymbol{\omega} \times \mathbf{x}$. When $\boldsymbol{\omega}$ is zero, a solver applicable to non-rotating reference frame is recovered.

Flow is assumed to be fully turbulent and turbulence is modeled using the negative Spalart–Allmaras (SA-neg) model [20]. Compared to the original SA model [21], this avoids the clipping of the turbulent variable to a non-negative value which potentially prevents the full convergence of the nonlinear solver. The turbulence equation is discretized using the first-order accurate upwind scheme [22].

B. Spatial discretization

The governing equations are discretized using the method of lines and thus the spatial and temporal discretizations can be treated separately. The governing equations for the steady-state solution \mathbf{W} is

$$\mathbf{R}(\mathbf{W}) = \mathbf{0}, \quad (1)$$

where \mathbf{R} is the sum of fluxes and source terms associated with each control volume. Suppose control volume i has N flux faces with area S_{ik} for $k = 1, 2, \dots, N$. R_i then is

$$R_i(\mathbf{W}) = \sum_{k=1}^N (\mathbf{F}_c^r - \mathbf{F}_v) S_{ik} + \mathbf{F}_\omega V_i,$$

where V_i denotes the volume. The computation of the convective flux \mathbf{F}_c^r is based on a modification of the Roe flux scheme to account for the relative reference frame that is rotating with a constant angular velocity; while the viscous flux \mathbf{F}_v is the same as in the stationary reference frame.

C. Temporal discretization for steady solver

The Newton method solves the steady-state nonlinear equation (1) iteratively as

$$\mathbf{W}^{n+1} = \mathbf{W}^n + \beta \Delta \mathbf{W}$$

until convergence is reached, i.e., $\|\mathbf{R}(\mathbf{W})\| = 0$, where $\Delta\mathbf{W}$ is the solution to the linear system of equations

$$\frac{\partial \mathbf{R}}{\partial \mathbf{W}} \Delta \mathbf{W} = -\mathbf{R}(\mathbf{W}^n),$$

while β is an under-relaxation factor obtained using a line search.

Once the spatial discretization, $\mathbf{R}(\mathbf{W}^n)$, is established, there are three main steps to complete a Newton update step, namely, (i) forming the Jacobian matrix, (ii) solving the large sparse linear system of equations, and (iii) finding a step size β and update the nonlinear flow solution. To form the Jacobian matrix, automatic differentiatino tool Tapenade [23] is used, together with graph coloring tool Colpack [24]. By executing the foward-differentiated residual subroutine for a subsets of nodes with the same color, the Jacobian matrix is calculated. The resulting large sparse linear system of equations is solved using GMRES right-preconditioned by the incomplete LU factorization with zero fill-in.

D. Temporal discretization for unsteady solver

III. Global linear stability analysis via eigenmode decomposition

A. Global linear stability analysis

The time-dependent RANS equations, discretized using the method of lines, is of the following form

$$\frac{d\mathbf{u}(t)}{dt} = \mathbf{R}(\mathbf{u}(t)) \quad (2)$$

where $\mathbf{u}(t)$ is vector of the time-varying conservative flow variables and $\mathbf{R}(\mathbf{u})$ is the nonlinear residual representating the spatial discretization. Note that the residual vector has already the volume of the cell taken into account, by diving the sum of the fluxes out of each cell by its volume. Assuming a steady state solution \mathbf{u}_0 (equilibrium point of the dynamic system) exists, and the time-varying flow variable can be decomposed into the steady and the unsteady part

$$\mathbf{u}(t) := \mathbf{u}_0 + \tilde{\mathbf{u}}(t)$$

. Assuming the perturbation is small, then and the governing equation becomes

$$\frac{d\tilde{\mathbf{u}}(t)}{dt} = A\tilde{\mathbf{u}}(t)$$

where A is the Jacobian $A := \frac{\partial \mathbf{R}}{\partial \mathbf{u}}$.

In order to use the eigen model decomposition approach, suppose matrix A has right eigenvectors $\{\mathbf{v}_1, \mathbf{v}_2, \dots, \mathbf{v}_N\}$,

which forms the matrix V as its column vectors. Matrix A can then be factorized as

$$A = V\Lambda V^{-1}$$

where the diagonal matrix Λ has the eigenvalues of the matrix A as its diagonal elements. Decomposing the unsteady part $\tilde{\mathbf{u}}$ in the eigen modal space with coordinates $\eta := \{\eta_1, \eta_2, \dots, \eta_N\}$,

$$\tilde{\mathbf{u}}(t) = V\eta(t).$$

Substituting $\tilde{\mathbf{u}}$ in the governing equation using the eigen modal decomposition, it becomes

$$\frac{d\eta(t)}{dt} = \Lambda\eta(t).$$

All equations are decoupled now and can be written as

$$\frac{d\eta_i(t)}{dt} = \lambda_i\eta_i(t) \quad \forall i.$$

For the linear system to be stable, a sufficient condition is that all eigenvalues have negative real parts, i.e., $\text{real}(\lambda_i) < 0, \forall i$.

B. Relation with time-accurate unsteady analysis

The relation between the eigenvalue and the time-accurate unsteady analysis is discussed in this subsection. Assume that the backward-differentiation-formula 1 (BDF1) is used. The discretized system is then

$$\frac{\eta_i^{n+1} - \eta_i^n}{T} = \lambda_i\eta_i^{n+1} \quad (3)$$

which yields

$$\eta_i^{n+1} = \frac{1}{1 - T\lambda_i}\eta_i^n \quad (4)$$

which means that for η_i to converge to zero, the amplification factor has to have a modulus smaller than 1, i.e.,

$$\left| \frac{1}{1 - T\lambda_i} \right| < 1$$

or equivalently,

$$|1 - T\lambda_i| > 1$$

The stability region is shown in the red part of the plot in

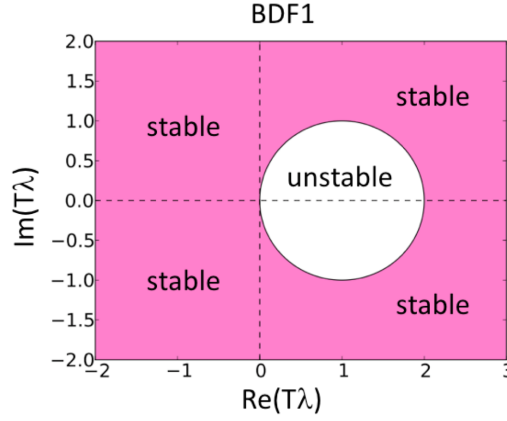


Fig. 1 123

If BDF2 is used, then the discretized equation becomes

$$\frac{3\eta_i^{n+2} - 4\eta_i^{n+1} + \eta_i^n}{2T} = \lambda_i \eta_i^{n+2} \quad (5)$$

Assuming the amplification factor is $z \in \mathbb{C}$, and substitute $\eta^{n+2} = z^2 \eta^n$ and $\eta^{n+1} = z \eta^n$ into eqn, one has the characteristic polynomial that equals zero:

$$(3 + 2T\lambda_i)z^2 - 4z + 1 = 0$$

and the stability region for $T\lambda_i$ can thus be defined as one such that $|z| < 1$, which is visualized in the figure

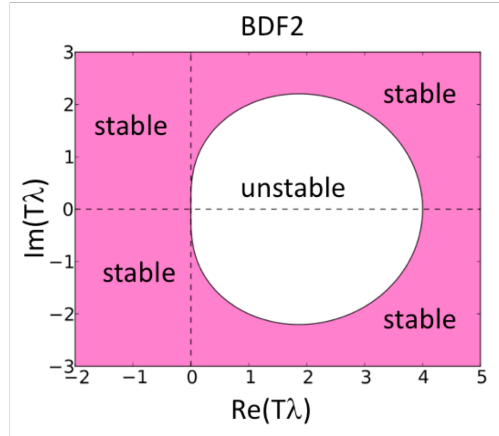


Fig. 2 123

Based on the stability analysis for the 1-step and 2-step backward differentiation formula (BDF), the following conclusions can be drawn regarding its relation to the eigenvalue analysis of the Jacobian matrix A for the spatial discretization.

- 1) if the matrix A has unstable eigehvalues (those that have positive real parts), then the time-stepping method with

a sufficiently small time-step should also exhibit linear instability (eigenvalues of the timestepping matrix lying outside the unit circle).

- 2) if all eigenvalues of the matrix A have negative real part, then the time-stepping method unconditionally stable, i.e., a small perturbation will decay and diminish.

C. Matrix structure for configurations with cyclic symmetry

1. circulant matrix

Consider the simplest case of a circulant matrix B

$$B = \text{circ}(b_0, b_1, \dots, b_{M-1}) = \begin{bmatrix} b_0 & b_1 & b_2 & \cdots & b_{M-2} & b_{M-1} \\ b_{M-1} & b_0 & b_1 & \cdots & b_{M-3} & b_{M-2} \\ \vdots & \vdots & \vdots & \vdots & \vdots & \vdots \\ b_1 & b_2 & b_3 & \cdots & b_{M-1} & b_0 \end{bmatrix}$$

Due to the cyclic symmetry, it can be verified that matrix B has M eigenvalues and eigenvectors defined as

$$\mathbf{v}_j = [1, \rho_j, \rho_j^2, \dots, \rho_j^{M-1}]^T, \quad \lambda_j = \sum_{m=0}^{M-1} b_m \rho_j^m \quad i = 0, 1, 2, \dots, M-1$$

Further more, it can be verified that all the eigenvectors are orthogonal to each other.

2. block-circulant matrix

A slightly more complex case is when each element in the circulant matrix is replaced at a block matrix, e.g., b_m is now an $N \times N$ square matrix, resulting in a block-circulant matrix.

Consider a vector \mathbf{w} of the following form:

$$\mathbf{w} = [\mathbf{v}, \rho \mathbf{v}, \rho^2 \mathbf{v}, \dots, \rho^{n-1} \mathbf{v}]^T$$

where ρ is any M -th root of 1 and \mathbf{v} is a vector of length N .

In order for \mathbf{w} to be the eigenvector of the block-circulant matrix B , the following equation has to be satisfied:

$$B\mathbf{w} = \lambda \mathbf{w}$$

which can be expanded as follows

$$\begin{aligned}
(b_0 + \rho b_1 + \rho^2 b_2 + \dots + \rho^{M-1} b_{M-1})\mathbf{v} &= \lambda \mathbf{v} \\
(b_{M-1} + \rho b_0 + \rho^2 b_1 + \dots + \rho^{M-1} b_{M-2})\mathbf{v} &= \lambda \rho \mathbf{v} \\
(b_{M-2} + \rho b_{M-1} + \rho^2 b_0 + \dots + \rho^{M-1} b_{M-3})\mathbf{v} &= \lambda \rho^2 \mathbf{v} \\
&\dots = \dots \\
(b_1 + \rho b_2 + \rho^2 b_3 + \dots + \rho^{M-1} b_0)\mathbf{v} &= \lambda \rho^{M-1} \mathbf{v}.
\end{aligned}$$

It can be seen that all rows are identical to the first row, different only by a scalar multiplication. λ and \mathbf{v} can be found by solving the eigenvalue problem of the equation in the first row. There are N \mathbf{v} for each ρ . When ρ varies from ρ_0 to ρ_{M-1} , a total of $N \times M$ \mathbf{v} can be found. The (m, n) -th of them is

$$\mathbf{w}_{m,n} = [\mathbf{v}_{m,n}, \rho_m \mathbf{v}_{m,n}, \rho_m^2 \mathbf{v}_{m,n}, \dots, \rho_m^{M-1} \mathbf{v}_{m,n}]^T$$

where $\mathbf{v}_{m,n}$ is the n -th eigenvalue of

$$(b_0 + \rho b_1 + \rho^2 b_2 + \dots + \rho^{M-1} b_{M-1})\mathbf{v} = \lambda \mathbf{v}$$

with $\rho = \rho_m$.

3. linearized discreted RANS equation in axisymmetric domain

The residual vector of the discreted RANS equation \mathbf{R} is linearized with respect to the flow variable \mathbf{U} to arrive at the full Jacobian matrix $\frac{\partial \mathbf{R}}{\partial \mathbf{U}}$, which describes the dynamic behavior of the system around the equilibrium point. It turns out that the fact that the computational domain has a cyclic symmetry can be exploited to reveal some characteristics of the eigenspace of the full Jacobian.

To facilitate the following discussion, it is assumed that the computational mesh, and thus the spatial discretization, is cyclic symmetric with M -periodicity, with M being the number of blades/passages in the entire annulus. Consequently, the full-annulus mesh can be divided into M non-overlapping segments, each of which contains N grid points. The grid points are ordered in such way that points $1 + N \times m$ to $N + N \times m$, $m = 0, 1, 2, \dots, M-1$ belongs to the m -th segment. In addition, the location of point $n + N \times m1$ (the n -th point in segment $m1$) is point $n + N \times m2$ (the n -th point in segment $m2$) rotated by an angle $(m2 - m1) \times 2\pi/M$. The arrangement of the grid point is illustrated in the following figure.

The entire Jacobian matrix then can be partitioned into the following block matrix

$$\frac{\partial \mathbf{R}}{\partial \mathbf{U}} = \begin{bmatrix} \frac{\partial \mathbf{R}_0}{\partial \mathbf{U}_0} & \frac{\partial \mathbf{R}_0}{\partial \mathbf{U}_1} & \frac{\partial \mathbf{R}_0}{\partial \mathbf{U}_2} & \cdots & \frac{\partial \mathbf{R}_0}{\partial \mathbf{U}_{M-1}} \\ \frac{\partial \mathbf{R}_1}{\partial \mathbf{U}_0} & \frac{\partial \mathbf{R}_1}{\partial \mathbf{U}_1} & \frac{\partial \mathbf{R}_1}{\partial \mathbf{U}_2} & \cdots & \frac{\partial \mathbf{R}_1}{\partial \mathbf{U}_{M-1}} \\ \vdots & \vdots & \vdots & \cdots & \vdots \\ \frac{\partial \mathbf{R}_{M-1}}{\partial \mathbf{U}_0} & \frac{\partial \mathbf{R}_{M-1}}{\partial \mathbf{U}_1} & \frac{\partial \mathbf{R}_{M-1}}{\partial \mathbf{U}_2} & \cdots & \frac{\partial \mathbf{R}_{M-1}}{\partial \mathbf{U}_{M-1}} \end{bmatrix} \quad (6)$$

where each block $\frac{\partial \mathbf{R}_{m_1}}{\partial \mathbf{U}_{m_2}}$, $m_1, m_2 = 0, 1, \dots, M-1$, is itself an $5N \times 5N$ matrix for Euler/laminar or $6N \times 6N$ matrix for turbulent flow modelled using a one-equation turbulence model. It can also be seen that each block is non-zero only when m_1 and m_2 either are identical or differ by 1. However, this property is not exploited in this subsection.

By changing the frame of reference to different pitchwise position, it can be shown that the matrix can be rewritten as

$$\frac{\partial \mathbf{R}}{\partial \mathbf{U}} = \begin{bmatrix} \frac{\partial \mathbf{R}_0}{\partial \mathbf{U}_0} & \frac{\partial \mathbf{R}_0}{\partial \mathbf{U}_1} & \frac{\partial \mathbf{R}_0}{\partial \mathbf{U}_2} & \cdots & \frac{\partial \mathbf{R}_0}{\partial \mathbf{U}_{M-1}} \\ B \frac{\partial \mathbf{R}_0}{\partial \mathbf{U}_{M-1}} B^{-1} & B \frac{\partial \mathbf{R}_0}{\partial \mathbf{U}_0} B^{-1} & B \frac{\partial \mathbf{R}_0}{\partial \mathbf{U}_1} B^{-1} & \cdots & B \frac{\partial \mathbf{R}_0}{\partial \mathbf{U}_{M-2}} B^{-1} \\ \vdots & \vdots & \vdots & \cdots & \vdots \\ B^{M-1} \frac{\partial \mathbf{R}_0}{\partial \mathbf{U}_1} B^{-(M-1)} & \frac{\partial \mathbf{R}_0}{\partial \mathbf{U}_2} B^{-(M-1)} & \frac{\partial \mathbf{R}_0}{\partial \mathbf{U}_3} B^{-(M-1)} & \cdots & B^{M-1} \frac{\partial \mathbf{R}_0}{\partial \mathbf{U}_0} B^{-(M-1)} \end{bmatrix} \quad (7)$$

Next, the following change of variable is used:

$$\tilde{\mathbf{U}}_i = B^{-i} \mathbf{U}_i, \quad \tilde{\mathbf{R}}_i = B^{-i} \mathbf{R}_i, \quad i = 0, 1, 2, \dots, M-1$$

The Jacobian then becomes

$$\frac{\partial \mathbf{R}}{\partial \mathbf{U}} = \begin{bmatrix} \frac{\partial \tilde{\mathbf{R}}_0}{\partial \tilde{\mathbf{U}}_0} & \frac{\partial \tilde{\mathbf{R}}_0}{\partial \tilde{\mathbf{U}}_1} B^{-1} & \cdots & \frac{\partial \tilde{\mathbf{R}}_0}{\partial \tilde{\mathbf{U}}_{M-1}} B^{-(M-1)} \\ B \frac{\partial \tilde{\mathbf{R}}_0}{\partial \tilde{\mathbf{U}}_{M-1}} & B \frac{\partial \tilde{\mathbf{R}}_0}{\partial \tilde{\mathbf{U}}_0} B^{-1} & \cdots & B \frac{\partial \tilde{\mathbf{R}}_0}{\partial \tilde{\mathbf{U}}_{M-2}} B^{-(M-1)} \\ \vdots & \vdots & \cdots & \vdots \\ B^{M-1} \frac{\partial \tilde{\mathbf{R}}_0}{\partial \tilde{\mathbf{U}}_1} & B^{M-1} \frac{\partial \tilde{\mathbf{R}}_0}{\partial \tilde{\mathbf{U}}_2} B^{-1} & \cdots & B^{M-1} \frac{\partial \tilde{\mathbf{R}}_0}{\partial \tilde{\mathbf{U}}_0} B^{-(M-1)} \end{bmatrix} \quad (8)$$

$$= \underbrace{\begin{bmatrix} I & 0 & \cdots & 0 \\ 0 & B & \cdots & 0 \\ \vdots & \vdots & \cdots & \vdots \\ 0 & 0 & \cdots & B^{M-1} \end{bmatrix}}_{\mathcal{B}} \underbrace{\begin{bmatrix} \frac{\partial \tilde{\mathbf{R}}_0}{\partial \tilde{\mathbf{U}}_0} & \frac{\partial \tilde{\mathbf{R}}_0}{\partial \tilde{\mathbf{U}}_1} & \cdots & \frac{\partial \tilde{\mathbf{R}}_0}{\partial \tilde{\mathbf{U}}_{M-1}} \\ \frac{\partial \tilde{\mathbf{R}}_0}{\partial \tilde{\mathbf{U}}_{M-1}} & \frac{\partial \tilde{\mathbf{R}}_0}{\partial \tilde{\mathbf{U}}_0} & \cdots & \frac{\partial \tilde{\mathbf{R}}_0}{\partial \tilde{\mathbf{U}}_{M-2}} \\ \vdots & \vdots & \cdots & \vdots \\ \frac{\partial \tilde{\mathbf{R}}_0}{\partial \tilde{\mathbf{U}}_1} & \frac{\partial \tilde{\mathbf{R}}_0}{\partial \tilde{\mathbf{U}}_2} & \cdots & \frac{\partial \tilde{\mathbf{R}}_0}{\partial \tilde{\mathbf{U}}_0} \end{bmatrix}}_{\mathcal{A}} \underbrace{\begin{bmatrix} I & 0 & \cdots & 0 \\ 0 & B^{-1} & \cdots & 0 \\ \vdots & \vdots & \cdots & \vdots \\ 0 & 0 & \cdots & B^{-(M-1)} \end{bmatrix}}_{\mathcal{B}^{-1}} \quad (9)$$

$$= \mathcal{B} \mathcal{A} \mathcal{B}^{-1} \quad (10)$$

Therefore the Jacobian matrix is similar to a block-circulant matrix \mathcal{A} . As forementioned, matrix \mathcal{A} has eigenvalues λ and eigenvectors \mathbf{w} . \mathbf{w} is a compound vector formed by assembling \mathbf{v} with scalar factor ρ . The eigenvector of $\frac{\partial \mathbf{R}}{\partial \mathbf{U}}$ can be easily obtained by left multiplying the \mathbf{w} with \mathcal{B} . Finally, the eigenvectors of the Jacobian matrix is

$$\mathbf{w}_{m,n} = [\mathbf{v}_{m,n}, \rho_m B \mathbf{v}_{m,n}, \rho_m^2 B^2 \mathbf{v}_{m,n}, \dots, \rho_m^{M-1} B^{M-1} \mathbf{v}_{m,n}]^T$$

where $\mathbf{v}_{m,n}$ is the n -th eigenvector of

$$\left(\frac{\partial \mathbf{R}_0}{\partial \mathbf{U}_0} + \rho \frac{\partial \mathbf{R}_0}{\partial \mathbf{U}_1} + \rho^2 \frac{\partial \mathbf{R}_0}{\partial \mathbf{U}_2} + \cdots + \rho^{M-1} \frac{\partial \mathbf{R}_0}{\partial \mathbf{U}_{M-1}} \right) \mathbf{v} = \lambda \mathbf{v}$$

with $\rho = \rho_m$. It can be seen that for a given n , the M eigenvectors $\mathbf{w}_{0,n}, \mathbf{w}_{1,n}, \dots, \mathbf{w}_{M-1,n}$ are modes with nodal diameters from 0 to $M-1$, or $1-M/2$ to $M/2$, provided that M is an even number.

D. Numerical implementation of eigenanalysis

In theory, performing the global linear stability analysis as described above is a standard procedure involving three steps: (i) find an equilibrium point \mathbf{u}_0 ; (ii) linearize the nonlinear residual and form the Jacobian matrix A , and (iii) perform eigenanalysis and find Λ and V . Step (i) is simply running the steady state flow solver until a steady state solution is found. Step (ii) is a by-product of the nonlinear flow calculation using the NK method, i.e., store away the Jacobian matrix at the final Newton step. Step (iii) is a bit more involved for high dimensional problems.

For eigenmode computations, the implicitly restarted Arnoldi method proposed by Sorensen [15] and implemented in the ARPACK library [16], is used in combination with the NutsCFD solver. Shift-and-invert spectral transformation is applied to converge to wanted parts of the eigenspectrum, and critical is therefore the robust solution of many linear systems of equations. Key to efficiently solving the arising large sparse linear system of equations is the deflated Krylov subspace solver GCRO-DR [25]. Compared with the more commonly used GMRES solver [26], GCRO-DR is both more CPU time and memory efficient, especially as the system matrix condition worsens, as demonstrated in [27, 28].

IV. Results

A. Laminar flow around a two-dimensional circular cylinder

Eigenvalue analysis is performed for the canonical case of the laminar flow around a circular cylinder with the Reynolds number in the range between 40 and 100. The computational domain is a circular cylinder centered at the origin with a diameter of $D = 10^{-5}$ and the farfield is a circle with a diameter of $100D$. The left half of the outer circle is set to 'farfield' boundary condition with an incoming flow of Mach 0.2 in the x-direction, a static pressure of 101325 Pa and a temperature of 288.15 K. The right half of the circle is set to 'pressure-outlet' boundary condition, with a constant pressure of 101325 Pa. The computational domain is meshed with quadrilateral elements, with a total of 29600 grid points. The density is 1.225 kg/m^3 . The dynamic viscosity is varied in order to achieve a particular Reynolds number.

1. Steady state calculation

The steady state flow solution for $Re = 55$ is obtained by either using an implicit solution method in Fluent (version 19.2) or by resorting to the Newton-Krylov algorithm in NutsCFD, despite the fact that the flow is physically unsteady under this condition. The Mach number contour of the NutsCFD calculation is shown in Fig. ??.

To compare the Fluent and NutsCFD results quantitatively, the x-velocity behind the cylinder and the pressure coefficient along the cylinder surface are presented in Fig. 3 and very good agreement can be found.

2. Unsteady calculation

Experimental results show that the laminar flow around the cylinder becomes unsteady for Re above a critical value (around 47)[29]. To study this phenomenon, unsteady flows for $Re = 55$ and $Re = 40$ are performed using NutsCFD. First, for both conditions, a steady state flow solution is obtained by converging the residual to machine error. Then, unsteady simulation is run with the steady state as the initial condition for $Re = 55$. A BDF2 second-order implicit dual-time-stepping method is used with the physical time step set to 10^{-8} sec , that is, 0.01 ms , and the inner loop is solved with a maximum of 3 Newton iterations. From Fig. 4, it can be seen that after around 100 ms , the lift coefficient starts to grow and eventually reaches a saturated limit cycle at around 130 ms . On the contrary, running unsteady simulation

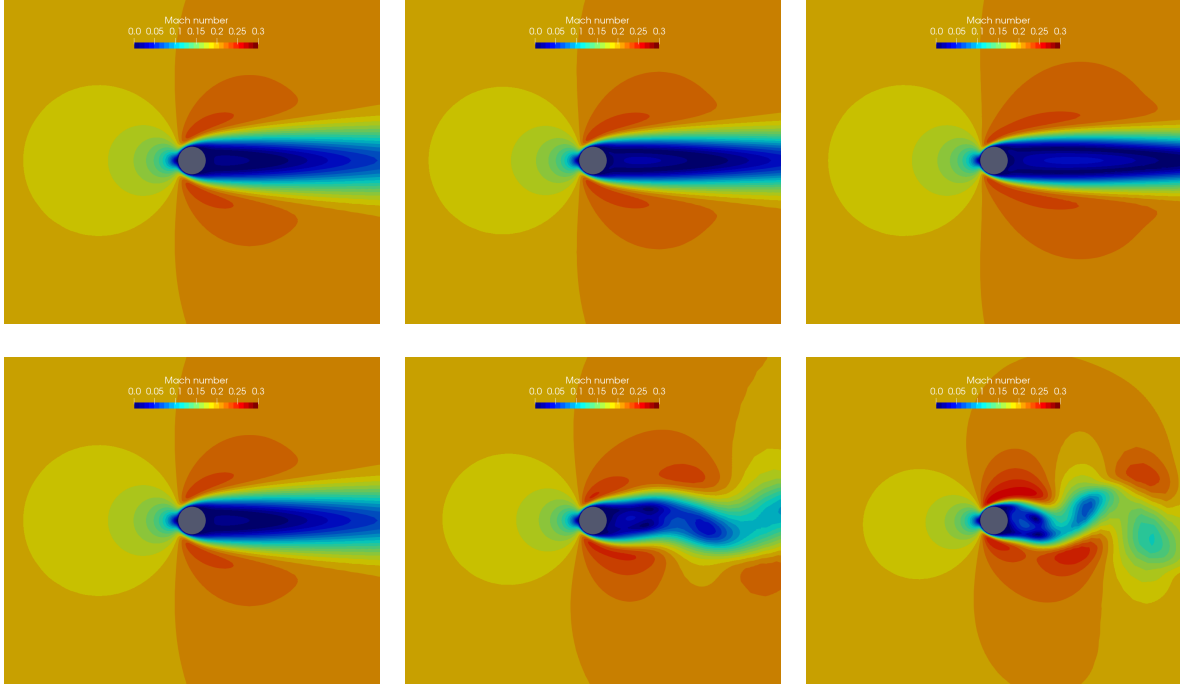


Fig. 3 From left to right: $Re=40, 60, 100$. Upper: steady state solution; lower: unsteady solution snapshot.

with a fully converged steady state for $Re = 40$ does not lead to unsteadiness. To probe the flow at $Re = 40$ further, a disturbance is introduced into the flow from the farfield by setting the incoming flow direction to vertical for one time step and switching it back to the x-direction, and then continue the unsteady run. The lift coefficient shows a transient growth but eventually slowly delays to zero. The two sets of lift coefficient signals for $Re = 40$ and $Re = 55$ are plotted in Fig. 4 in both linear and logarithmic scales. The logarithmic plot on the right clearly shows an exponential growth/decay for $Re = 55$ and $Re = 40$, respectively.

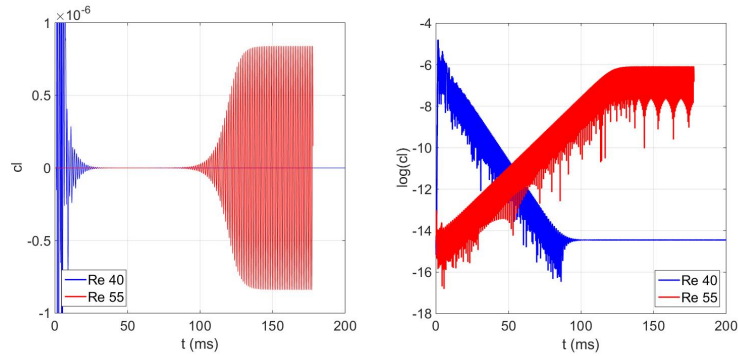


Fig. 4 Lift coefficient histogram for $Re = 55$ and $Re = 40$.

3. Eigenanalysis

Eigenanalysis is performed for the steady state solution calculated using NutsCFD. After converging the steady state solver to machine error ($tol = 10^{-14}$), the exact Jacobian matrix based on the 2nd-order spatial accuracy is calculated and output to file. **ARPACK** is used to compute a subset of the eigenvalues, with the aim of finding the least stable mode. To minimize the computational effort, 10 eigenvalues/vectors are computed for matrices with different shifts of 0, i , $2i$, $3i$, $4i$, $5i$. All the eigenvalues, 60 in total and with some duplicated, are plotted in Fig. 5. It can be seen that there is one eigenvalue that is on the right side of the imaginary axis, indicating there is one unstable mode. In the meantime, from the time-domain simulation, one can extract from the lift-coefficient signal that the flow is exponentially growing with a growth rate of 0.123 and oscillating with a circular frequency of 4.94 rad/s. This value is plotted along with the spectrum and it can be seen that it overlaps with the unstable eigenvalue from the eigenanalysis.

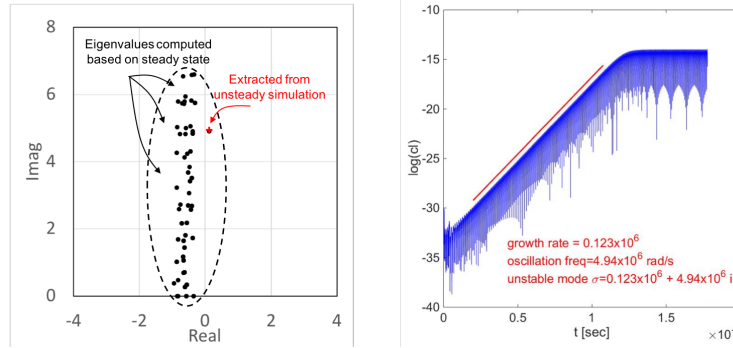


Fig. 5 Eigenspectrum from the steady state eigenvalue analysis compared with the linearly destabilizing unsteady simulation for $Re = 55$.

The eigenanalysis not only generates the eigenvalues but also the eigenvectors associated with each eigenvalue. For the unstable mode, the real part of the density, x/y momentum and energy component of the unstable eigenvector is shown in Fig.6. Although not further explored here, these eigenvectors will be useful for constructing reduced-order-models, which can be used for rapid parametric study or fast time-domain response.

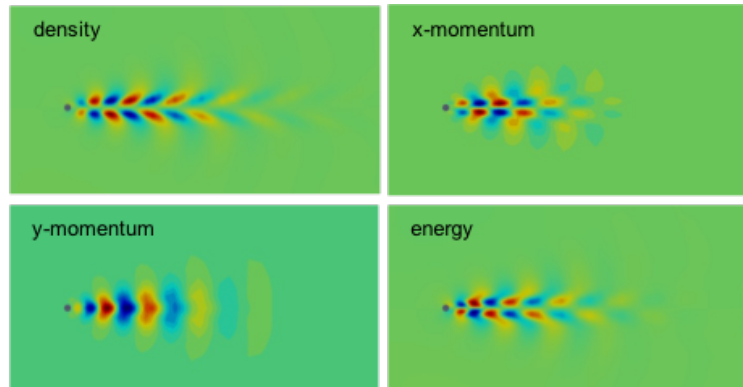


Fig. 6 Real part of the density, x/y momentum, energy components of the unstable eigenmode for $Re = 55$.

4. Bifurcation tracking

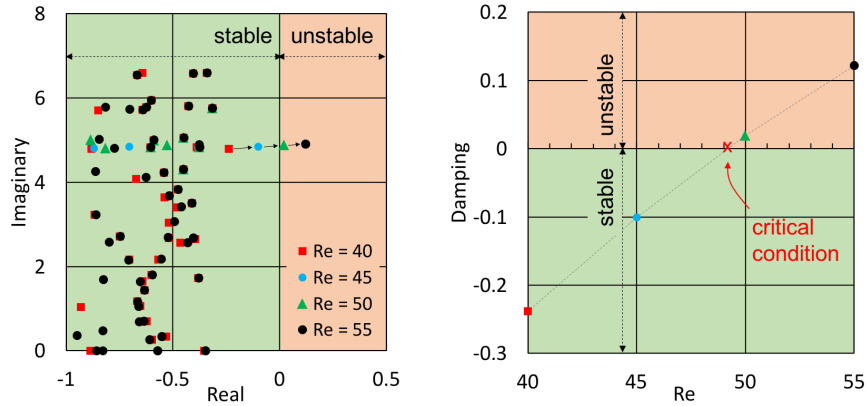


Fig. 7 The spectra for $Re = 40, 45, 50$ and 55 (left) and the damping v.s. the Reynolds number (right).

The same procedure for computing the eigenvalues for $Re = 55$ is applied to flows at $Re = 40, 45$, and 50 to obtain their respective spectra, which is shown in Fig. 7. It can be seen that as the bifurcation parameter Re is increased from 40 to 55 , one eigenmode becomes linear unstable. The real part of this eigenvalue is plotted against Re on the right in Fig. 7. It crosses the imaginary axis at approximately $Re = 49$, consistent with the experimental value of $Re_{crit} = 47$. Note that shown in the figure is only the upper half of the spectrum and the complex conjugate of the destabilizing eigenvalue is thus not visualized. This is a classic Hopf bifurcation as the conjugate complex eigenpair destabilizes simultaneously. However, it should be noted that although linear stability analysis can predict the exact bifurcation, frequency predicted based on the unstable eigenvalue beyond that critical bifurcation parameter, Re_{crit} , should be used with care as it is different from the vortex shedding frequency except very close to onset, for the laminar flow around a long cylinder [30]. The implication on general cases is yet to be explored in future work.

B. Singlerow annular cascade (quasi-3D analysis)

NutsCFD is used to analyze the performance of the first stage rotor (NASA Rotor 67) of a two stage transonic fan designed and tested at the NASA Glenn center [31]. Its design pressure ratio is 1.63 , at a mass flow rate of 33.25 kg/sec. The NASA Rotor 67 has 22 blades with tip radii of 25.7 cm and 24.25 cm at the leading and trailing edge, respectively, and a constant tip clearance of 1.0 mm. The hub to tip radius ratio is 0.375 at the leading edge ($TC = 0.6\%$ span) and 0.478 at the trailing edge ($TC = 0.75\%$ span). The design rotational speed is $16,043$ RPM, and the tip leading edge speed is 429 m/s with a tip relative Mach number of 1.38 .

As a first step, the analysis is performed on the surface of revolution taken at approximately 50% of the blade height. The three-dimensional mesh has one cell in the radial direction and the subsequent analysis is thus a quasi-3D one.

1. Steady state calculation

Steady state analysis is first performed for an annular compressor cascade. The pressure ratio and efficiency against the mass flow normalized by the choked mass flow, produced by incrementally raising the back pressure, are shown in Fig. ?? . The fully-converged steady state flow solution corresponding to the lowest and highest back pressures are shown in Fig. 9.

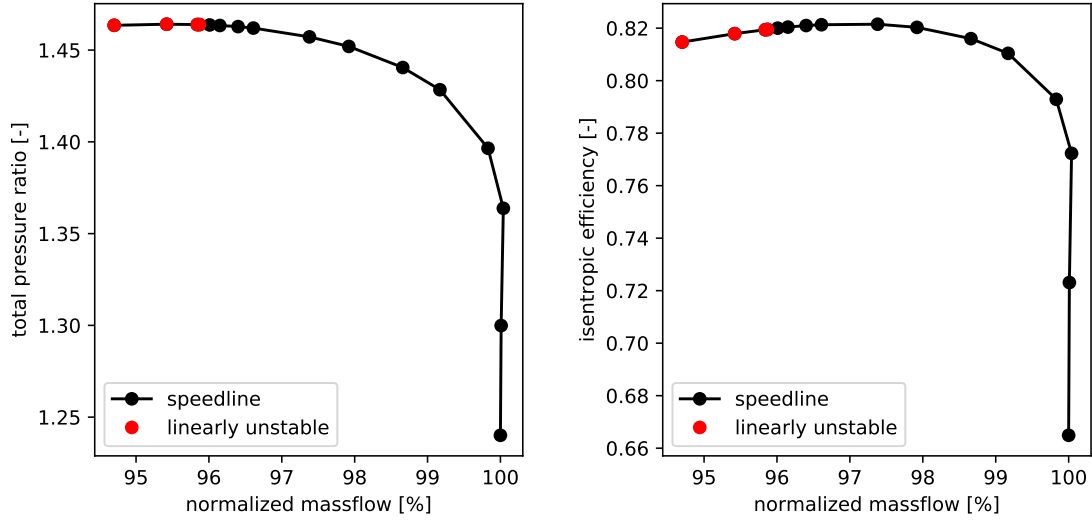


Fig. 8

2. Eigenanalysis

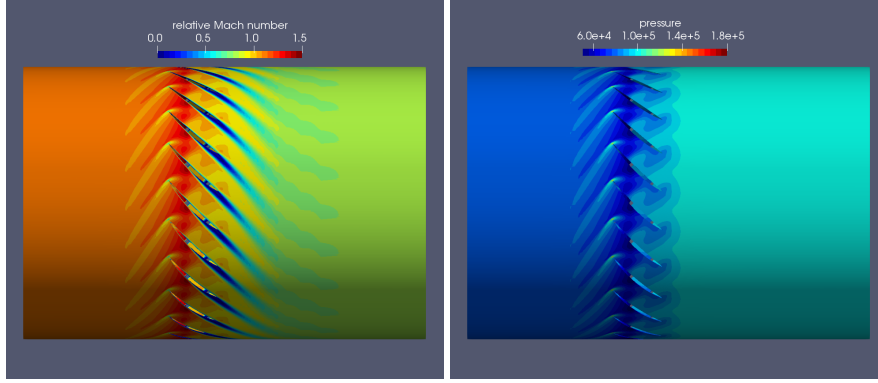
Eigenvalue analysis is performed for all the steady state solutions along the speedline. Since only the 'relevant' eigenvalues are desired (relevant here means eigenvalues that are likely to across the imaginary axis, corresponding to the onset of Hopf-bifurcation), the knowledge that the rotating stall cells usually move along the circumferential direction with a speed that is on the same order of the rotating rotation speed, each element of the Jacobian matrix is therefore divided by a factor of $1/(2\pi \times 16043/60) \approx 1/1680$ (assuming the rotational speed of 16,043 RPM), so that the frequency information represented by the imaginery part of the eigenvalues found is in terms of engine order (EO).

For each condition in Fig. 9, the relevant eigenvalues are computed by applying shifts of $\sigma = 0 + 0.5j, 0 + 1j, 0 + 1.5j$ and $0 + 2j$ to the Jacobian matrices and finding the 10 most interior eigenvalues of the shifted matrices.

3. Interpretation of the eigenanalysis results

Shown in Fig. 10 is a subset of the eigenvalues that are near the imaginary axis, which presumably are most likely to be unstable. ARPACK is used with various imaginery shifts to compute interior eigenvalues. The ones that are suspicious of crossing the imaginery axis are shown. A zoomed view of the eigenvalues reveals that there are a total of

choked condition



near stall condition

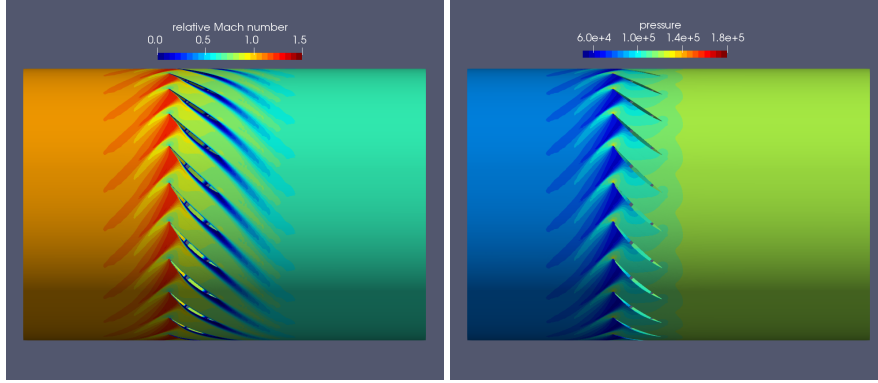


Fig. 9 Pressure (left) and SA variable (right) contours for whole-annulus calculations.

five that have positive real parts, i.e., unstable. A single-mode instability is not found for the case most likely because the flow condition chosen is one that is deep into the linearly unstable region and a bifurcation point should be searched for at a higher flow-rate condition. Nevertheless, in the work, we restrict ourselves to the analysis of this single condition and a thorough exploration of the whole picture will be conducted in our future work.

The unstable eigenvector with the smallest imaginary part (lowest point among the five unstable eigenvalues) is visualized in Fig. 12 with both the real and imaginary parts. The circumferential shock oscillation can be seen. To analyze the spatial modes, data along the intersecting curve is taken (marked at the red line in Fig. 12). This is done for each of the 11 modes (marked with red cross in Fig. 10). It is clear from the spatial Fourier analysis that each eigenvector corresponds to a rotating pattern with a different nodal diameter, which increases from 1 to 11 monotonically from the lowest to the highest eigenvalues.

A more involved data processing reveals that the perturbation pattern, for every eigenvector, is a travelling wave that rotates in the opposite direction of the motion of the rotor (in the relative frame), and with a speed a fraction of the shaft rotating speed. This relative rotating speed can be calculated using the imaginary of the eigenvalue and the nodal

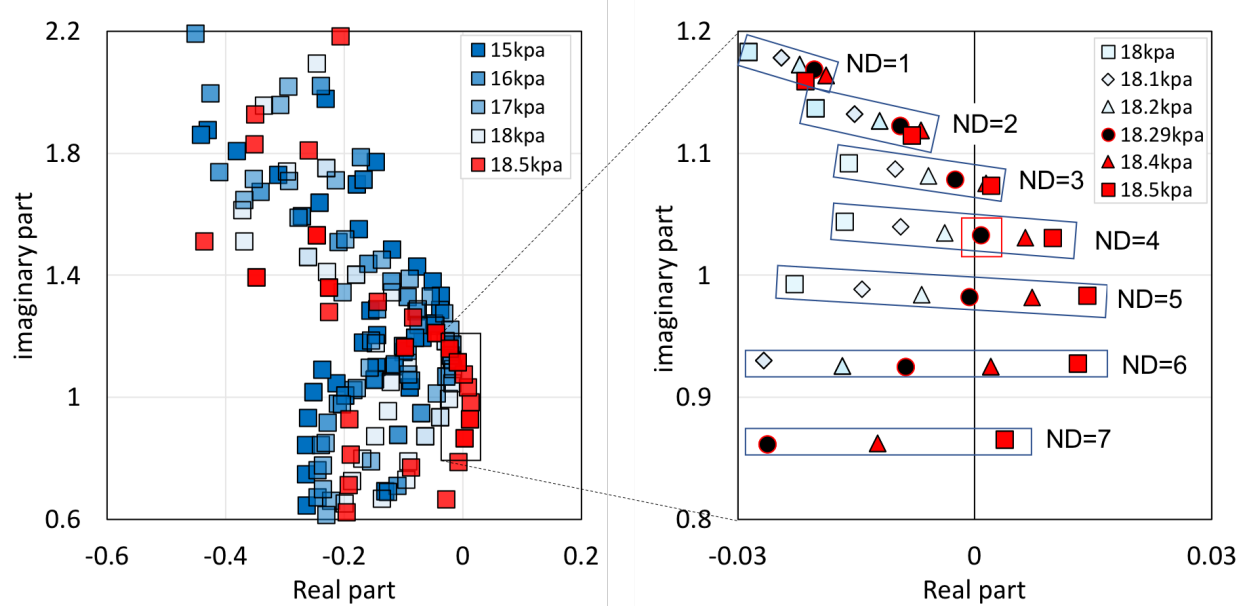


Fig. 10 Spectrum for stall condition.

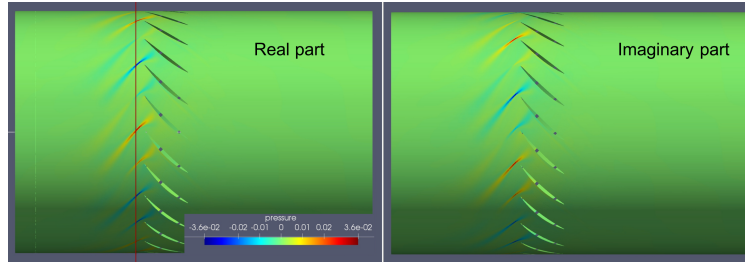


Fig. 11 Eigenvector 5 visualized using the real and imaginary parts of energy component

diameter of the perturbation pattern as

$$\Omega_{cellRotation}^{rel} = \frac{\text{Imag}(\lambda)}{ND} \Omega_{shaft} \quad (11)$$

In the absolute reference frame, the cell rotating speed (normalized with shaft angular frequency) is calculated as

$$\Omega_{cellRotation}^{abs} = \left(1 - \frac{\text{Imag}(\lambda)}{ND}\right) \Omega_{shaft} \quad (12)$$

Applying this formula to each of the 11 eigenmodes leads to the correlation between the nodal diameter and the perturbation rotating speed, as shown in Fig. 12. Note that we use the terminology 'cell rotating speed' to be consistent with the language used by experimentalists when they describe the rotating cells. In fact, what is meant in the current context is actually 'rotating speed of the perturbation pattern'. Although it is well-known that the conclusions drawn from a global linear stability analysis can not represent the behavior of a saturated limit cycle which is highly

nonlinear, it seems that the characteristics of the rotating perturbation, in terms of nodal diameter and rotating speed, is qualitatively representative of rotating cells observed experimentally. However, questions such as which eigenmode should destabilizes first, and how does the inlet distortion and blade-row interaction in multirow configuration affect the conclusion, remain to be answered.

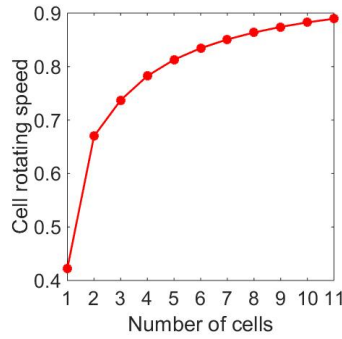


Fig. 12 The cell rotating speed in the absolute frame of reference v.s. the number of cells (nodal diameter of the perturbation pattern).

4. Unsteady analysis

C. Rotor 67

Update performance curve with data at the correct survey station location.

1. Case overview

The final case is the NASA Rotor 67 transonic fan, which is the first-stage rotor of a two-stage transonic fan. It has 22 low aspect-ratio blades and was designed for a rotational speed of 16,043 rpm, with a total pressure ratio of 1.63 and a mass flow of 33.25 kg/s [?]. The flow calculations for this case are performed using 72 processors.

2. Accuracy validation

The computational domain with a single blade passage is meshed with 973,065 grid points and 934,400 hexahedral elements. The height of the first layer cell off the viscous wall is 10^{-6} m, satisfying $y^+ \approx 1$. The geometry of the rotor blade as well as detailed views of the mesh are shown in Fig. 13.

At the inlet boundary, a total pressure of 101325 Pa and a total temperature of 288.15 K are imposed. The incoming flow is in the axial direction. Since the outlet boundary is relatively far from the rotor, i.e., the distance from the rotor trailing edge to the outlet boundary is over twice the chord length, a constant back pressure is imposed at the outlet as the boundary condition. Our numerical experiment shows that using a radial equilibrium boundary condition only changes the resulting speedline negligibly. Therefore, the constant back pressure boundary condition is used for simplicity. The back pressure is set to 0 kPa initially and then gradually raised to produce the speedline. The procedure illustrated in

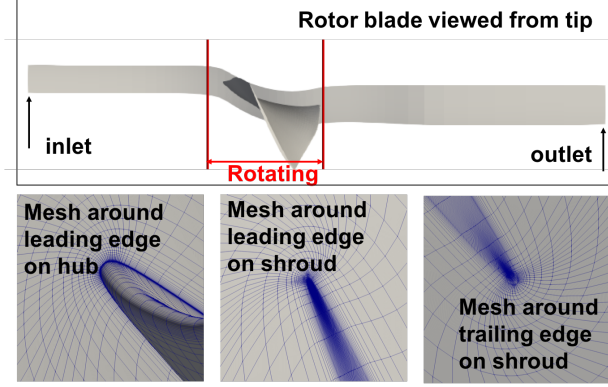


Fig. 13 NASA rotor 67 blade viewed from the tip (top) and detailed views of the computational mesh (bottom). The rotating part of the hub surface, from $x = -1.374$ cm to $x = 9.365$ cm, is marked with the two vertical lines.

Fig. ??, is used to generate the speedline, except that for this case, pressure increments of 5 kPa, 1 kPa and 0.1 kPa are used.

The experimental and numerical speedlines are shown in Fig. 14 for comparison. The relative error for the choked flow rate is 1.0%, which is similar to reported values of other numerical investigations [?]. The under-prediction of the pressure ratio and the efficiency is suspected to be caused by the fact that the implementation of the S-A turbulence model used here is not fully appropriate for this case. However, as this work focuses on the solver convergence and robustness, this is not further investigated here.

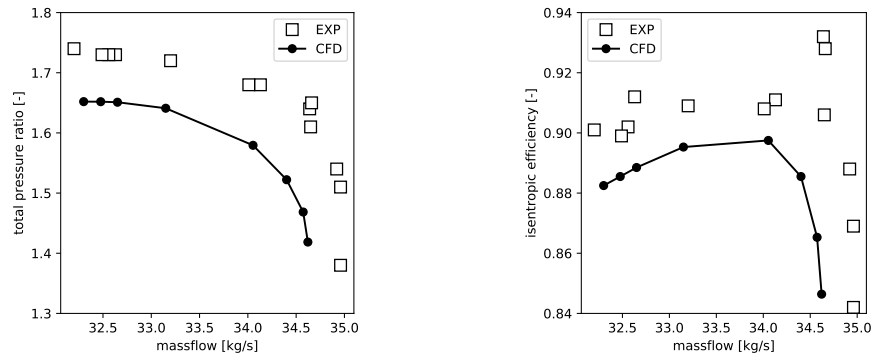


Fig. 14 CFD calculations compared with measurements [?] for NASA Rotor 67.

V. Conclusion

Rotating flow instability at near stall condition for an annular compressor cascade is studied using the eigenanalysis approach and the destabilizing eigenmodes are computed and analyzed to shed insight on the rotating stall phenomenon. This is the first time a full-order global linear stability analysis based on the three dimensional RANS equations is performed to study the destabilising mechanism of such turbomachinery flow phenomenon.

Specifically, a stable nonlinear flow solver based on the matrix-forming Newton–Krylov approach is used to compute the steady state flow solution at near stall (possibly post-stall) condition and the readily available exact Jacobian matrix is then used for eigenvalue analysis. The eigenanalysis is performed to compute a subset of the eigenvalues that are near the imaginary axis, with the implicit-restarted Arnoldi method implemented in the ARPACK library. The shift-and-invert approach is used to obtain the least unstable eigenvalues.

The methodology is first applied to the classic case of a laminar flow around a 2D circular cylinder. By perturbing the system parameter Re , Hopf bifurcation is identified which is responsible for the inception of the laminar vortex shedding. The frequency and linear growth ratio from the eigenanalysis agree well with time-dependent simulation during the linear growth regime.

The same procedure is then applied to the a quasi-3d compressor rotor. Analysis shows the existence of a complete set of spatial modes that have different nodal diameters and rotating speeds. These analysis results provide a solid foundation for the explanation of various observations in experiments regarding rotating flow instabilities. It is revealed that the multiple modes with different nodal diameters coexist, as the inherent property of the physical system, and it can be hypothesized that the reason for different observed stall cell patterns is due to one particular mode being excited to finite amplitude first by external disturbance. Further more, by processing the spatial modes and the imaginary part of the eigenvalues, rotating speeds of the perturbation patterns can be calculated and are found to qualitatively agree with the various experimentally observed values for rotating stall cells.

The preliminary results presented in this paper represent our first attempt to use eigenanalysis based on RANS equations to study the rotating flow instability phenomenon in turbomachinery flows. The results are promising in that it shows the eigenanalysis method is feasible for practical cases and the eigenvectors do capture some of the key features of the flow instability investigated. However, more in-depth study is needed to investigate the bifurcation process for the quasi-3D case, and further investigation into three-dimensional cases will be carried out in our future work.

Acknowledgements

This work received support by the National Natural Science Foundation of China (Grant No. 51790512).

References

- [1] Emmons, H., “Compressor surge and stall propagation,” *Trans. of the ASME*, Vol. 77, No. 4, 1955, pp. 455–467.
- [2] Marble, F. E., “Propagation of stall in a compressor blade row,” *Journal of the Aeronautical Sciences*, Vol. 22, No. 8, 1955, pp. 541–554.
- [3] Emmons, H., Kronauer, R., and Rockett, J., “A survey of stall propagation—experiment and theory,” *Journal of Basic Engineering*, Vol. 81, No. 3, 1959, pp. 409–416.

- [4] Cornelius, C., Biesinger, T., Galpin, P., and Braune, A., "Experimental and computational analysis of a multistage axial compressor including stall prediction by steady and transient CFD methods," *Journal of Turbomachinery*, Vol. 136, No. 6, 2014, p. 061013.
- [5] He, L., "Computational study of rotating-stall inception in axial compressors," *Journal of Propulsion and Power*, Vol. 13, No. 1, 1997, pp. 31–38.
- [6] Vo, H. D., Cameron, J. D., and Morris, S. C., "Control of short length-scale rotating stall inception on a high-speed axial compressor with plasma actuation," *ASME Turbo Expo 2008: Power for Land, Sea, and Air*, American Society of Mechanical Engineers, 2008, pp. 533–542.
- [7] Pullan, G., Young, A., Day, I., Greitzer, E., and Spakovszky, Z., "Origins and structure of spike-type rotating stall," *Journal of Turbomachinery*, Vol. 137, No. 5, 2015, p. 051007.
- [8] Greitzer, E., and Moore, F., "A theory of post-stall transients in axial compression systems: part II—application," *ASME J. Eng. Gas Turbines Power*, Vol. 108, No. 2, 1986, pp. 231–239.
- [9] Stenning, A., "Rotating stall and surge," *Journal of Fluids Engineering*, Vol. 102, No. 1, 1980, pp. 14–20.
- [10] Paduano, J., Epstein, A., Valavani, L., Longley, J., Greitzer, E., and Guenette, G., "Active control of rotating stall in a low speed axial compressor," *ASME 1991 International Gas Turbine and Aeroengine Congress and Exposition*, American Society of Mechanical Engineers, 1991, pp. V001T01A036–V001T01A036.
- [11] DAY, I., "Active Suppression of Rotating Stall and Surge in Axial Compressors," *J. Turbomach.*, Vol. 115, 1993, pp. 40–47.
- [12] Paduano, J. D., Greitzer, E., and Epstein, A., "Compression system stability and active control," *Annual review of fluid mechanics*, Vol. 33, No. 1, 2001, pp. 491–517.
- [13] Day, I., Breuer, T., Escuret, J., Cherrett, M., and Wilson, A., "Stall inception and the prospects for active control in four high speed compressors," *ASME 1997 International Gas Turbine and Aeroengine Congress and Exhibition*, American Society of Mechanical Engineers, 1997, pp. V004T15A022–V004T15A022.
- [14] Amestoy, P. R., Duff, I. S., L'Excellent, J.-Y., and Koster, J., "MUMPS: a general purpose distributed memory sparse solver," *International Workshop on Applied Parallel Computing*, Springer, 2000, pp. 121–130.
- [15] Sorensen, D. C., "Implicit application of polynomial filters in a k-step Arnoldi method," *SIAM journal on matrix analysis and applications*, Vol. 13, No. 1, 1992, pp. 357–385.
- [16] Lehoucq, R. B., Sorensen, D. C., and Yang, C., *ARPACK users' guide: solution of large-scale eigenvalue problems with implicitly restarted Arnoldi methods*, Vol. 6, SIAM, 1998.
- [17] Xu, S., Radford, D., Meyer, M., and Müller, J.-D., "Stabilisation of discrete steady adjoint solvers," *Journal of Computational Physics*, Vol. 299, 2015, pp. 175–195.

- [18] Day, I., “Stall, surge, and 75 years of research,” *Journal of Turbomachinery*, Vol. 138, No. 1, 2016, p. 011001.
- [19] Xu, S., Mohanamuraly, P., Wang, D., and Müller, J.-D., “A parallel Newton–Krylov RANS solver for turbomachinery aerodynamic analysis at off-design conditions,” *submitted*, 2019.
- [20] Allmaras, S. R., and Johnson, F. T., “Modifications and clarifications for the implementation of the Spalart–Allmaras turbulence model,” *Seventh international conference on computational fluid dynamics (ICCFD7)*, 2012, pp. 1–11.
- [21] Spalart, P. R., and Allmaras, S. R., “A one equation turbulence model for aerodynamic flows,” AIAA-CP 92-439, 1992.
- [22] Langer, S., “Agglomeration multigrid methods with implicit Runge–Kutta smoothers applied to aerodynamic simulations on unstructured grids,” *Journal of Computational Physics*, Vol. 277, 2014, pp. 72–100.
- [23] Hascoët, L., and Pascual, V., “The Tapenade Automatic Differentiation tool: Principles, Model, and Specification,” *ACM Transactions On Mathematical Software*, Vol. 39, No. 3, 2013.
- [24] Gebremedhin, A. H., Nguyen, D., Patwary, M. M. A., and Pothen, A., “ColPack: Software for graph coloring and related problems in scientific computing,” *ACM Transactions on Mathematical Software (TOMS)*, Vol. 40, No. 1, 2013, p. 1.
- [25] Parks, M., de Sturler, E., Mackey, G., Johnson, D., and Maiti, S., “Recycling Krylov subspaces for sequences of linear systems,” *SIAM Journal on Scientific Computing*, Vol. 28, No. 5, 2006, pp. 1651–1674.
- [26] Saad, Y., and Schultz, M., “GMRES: A generalized minimal residual algorithm for solving nonsymmetric linear systems,” *SIAM Journal on scientific and statistical computing*, Vol. 7, No. 3, 1986, pp. 856–869.
- [27] Xu, S., Timme, S., and Badcock, K., “Enabling off-design linearised aerodynamics analysis using Krylov subspace recycling technique,” *Computers & Fluids*, Vol. 140, 2016, pp. 385–396.
- [28] Xu, S., and Timme, S., “Robust and efficient adjoint solver for complex flow conditions,” *Computers & Fluids*, Vol. 148, 2017, pp. 26–38.
- [29] Williamson, C. H. K., “Vortex Dynamics in the Cylinder Wake,” *Annual Review of Fluid Mechanics*, Vol. 28, No. 1, 2003, pp. 477–539.
- [30] Barkley, D., “Linear analysis of the cylinder wake mean flow,” *Europhysics Letters*, Vol. 75, No. 5, 2006, p. 750.
- [31] Strazisar, A. J., Wood, J. R., Hathaway, M. D., and Suder, K. L., “Laser anemometer measurements in a transonic axial-flow fan rotor,” 1989.